Experimental Aerodynamics Applied to Separated and Vortical Flows

C. Breitsamter[1]
[1]Technical University of Munich, Department of Mechanical Engineering, Chair of Aerodynamics and Fluid Mechanics, Boltzmannstr. 15, 85748 Garching
GERMANY

christian.breitsamter@tum.de

ABSTRACT

An overview of measurement techniques and application scenarios is presented focusing on leading- and trailing-edge vortex flow development. Measurement data obtained for the Mach number range of interest are typically exploited for the analysis of global and local aerodynamic load characteristics as well as for the analysis of flow physics phenomena based on specific field quantities. Experimental data serve as reference data for numerical flow simulations. Today's high fidelity computational simulations require high quality experimental data of detailed flow field quantities to improve numerical schemes and, in particular, to set up and enhance numerical modeling related to transitional and turbulent flow. Similarity in Reynolds number may require cryogenic wind tunnel testing which substantially increases the effort on measurement equipment and test conduction. The present article briefly addresses standard measurement techniques to obtain aerodynamic forces and moments, surface pressures, flow field velocities and surface flow visualization. A special focus is on optical measurement systems including pressure sensitive paint, particle image velocimetry and photogrammetry for surface deformation analysis. Transition detection methods are addressed as well. Future directions concentrate on time-accurate and volumetric measurements enhancing continuously the capabilities of particle image velocimetry applications as well as on refinements of unsteady pressure sensitive paint methods, respectively.

NOMENCLATURE

b	Wing span, [m]
b_0	Lateral distance of rolled-up wake vortices, [m]
c_r	Wing root chord, [m]
C_D	Drag coefficient, [-]
C_p	Pressure coefficient, $C_p = (p - p_\infty)/q_\infty$, [-]
C'_p	Pressure coefficient fluctuations, [-]
$C_{p,rms}$	Root-mean-square pressure coefficient, [-]
f	Frequency, [Hz]
k	Reduced frequency, $k = (f\, l_\mu / U_\infty)$
l_μ	Mean aerodynamic chord, [m]
Ma	Mach number, free stream Mach number, [-]
p	Static pressure, [Pa]
p_∞	Free stream static pressure, [Pa]
q_∞	Free stream dynamic pressure, $q_\infty = (\rho_\infty/2)/ U^2_\infty$, [Pa]
Re	Reynolds number, [-]
Re_{mac}	Reynolds number based on mean aerodynamic chord, [-]
$S^N_{u'}$	Normalized power spectral density of axial velocity fluctuations, [-]

Tu_z	Turbulence intensity based on vertical velocity fluctuations, [-]
U_∞	Free stream velocity, [m/s]
V	Total velocity, [m/s]
u, v, w	Axial, lateral and vertical velocities, [m/s]
u', v', w'	Axial, lateral and vertical velocity fluctuations, [m/s]
x, y, z	Coordinates, [m]
x*, y*, z*	Non-dimensional coordinates, x* = x/b, [-]
α	Angle of attack, [deg]
α_{max}	Maximum angle of attack, [deg]
β	Angle of sideslip, [deg]
ρ_∞	Free stream density, [kg/m^3]
ξ	Non-dimensional axial vorticity, $\xi = (\omega_x (b/2))/ U_\infty$, [-]
Λ	Wing aspect ratio, [-]
λ	Wing taper ratio, [-]
φ_W	Leading-edge sweep angle, [deg]
ω_x	Axial vorticity, [1/s]
Im	Imaginary part
Re	Real part

1.0 INTRODUCTION

The wind tunnel is the typical test environment for aircraft and rotorcraft aerodynamics analysis reaching back to the Wright Brothers. Typically, a scaled model is used mounted in the wind tunnel test section assuming aerodynamic similarity between a body moving through the air in rest and a fixed body encountering a free stream velocity equal to the moving velocity. In general, wind tunnels are unique facilities designed for specific purposes and operating conditions. Wind tunnels are available for Mach number regimes from low subsonic to high supersonic speeds.

2.1 Wind Tunnel Testing

The classical wind tunnel types are the free jet type, Eiffel type or Göttingen type. The free jet type consists of a front fan, plenum chamber with honeycombs and turbulence screens, and the nozzle. The test article is located in front of the nozzle. The Eiffel type extends the jet type facility by a diffuser downstream of the (closed) test section placing the fan within the downstream duct. Thus, the impact of fan induced flow disturbances on the test section flow is alleviated. A diffuser part upstream and downstream of the fan diminishes energy consumption due to pressure recovery. Eiffel type wind tunnels may feature very large contraction ratios thus enabling laminar airfoil and wing testing due to very low free stream turbulence levels. Adding a closed return passage results in the Göttingen type wind tunnel. Corner turning vanes and return passage second and third diffuser sections are further design elements to close the duct in direction to the plenum chamber. If possible, the fan is located in the return passage with maximum distance to the test section to minimize the impact of fan related disturbances on the test section flow. Adding the return passage substantially decreases the fan power for a desired test section speed as the fan has only to compensate the

duct related losses. The test section can be of open or closed type. The latter may be fitted with a breather for atmospheric conditions or pressurized, e.g. for high Reynolds number testing. All components of the wind tunnel duct, i.e. plenum chamber with honeycombs and turbulence screens, nozzle, test section, diffusers, corner turning vanes, flow guiding elements, fan, straightener vanes, cooler devices, etc. are subject to detailed design and optimized for minimum losses. Further requirements may be due to aeroacoustic specifications. Göttingen-type wind tunnel facilities for aircraft testing cover the whole Mach number regime, namely low-speed, subsonic, transonic and supersonic speed. Among others, well-known facilities are e.g. DNW-LLF (German-Dutch Wind Tunnels, Large Low Speed Facility, Marknesse, The Netherlands), S1MA (ONERA, Modane, France), ETW (European Wind Tunnel Facility, Cologne, Germany) and NTF (National Transonic Facility, NASA Langley Research Center, Hampton, USA). Detailed information on low- and high-speed wind tunnel testing is given in Refs. [29] and [30].

Wind tunnel testing using scaled models experience fluid mechanics similarity requirements to exploit the small-scale data for the large-scale counterpart. Besides the geometric similarity and demands on model surface quality the identity in fluid mechanics similarity numbers is required. For aircraft model testing, these numbers usually comprise Reynolds number, Mach number, Eckert number, Prandtl number, Froude number and Strouhal number with a direct relation between Mach number and Eckert number for air flow. Regarding quasi-steady flow conditions, negligible influence of gravitational force and testing in air, the dominant similarity numbers are Mach number and Reynolds number. Mach number similarity results generally in smaller test section sizes because of the required fan power while Reynolds number similarity results in facilities with highly increased test section pressure or cryogenic facilities assuring also Mach number similarity. Cryogenic facilities offer a test section working temperature down to 110 K which implies Reynold numbers in the order of 10^7 to 10^8 with respect to reference lengths of transport type aircraft models at a scale of 1:20 to 1:35. Such facilities may allow to adjust Mach number, Reynolds number and dynamic pressure nearly independently within certain ranges meeting industrial requirements on today's high fidelity wind tunnel testing capabilities. There are quantities to judge the test section flow quality, typically with respect to temporal and spatial uniformity of the flow field, turbulence level, flow direction and pressure gradient [29], [32]. Wind tunnel data uncertainty is discussed for example in the advisory report AGARD-AR-304 [4]. A further important issue is related to correction methods applied for open and closed test section arrangements accounting for the difference of the wind tunnel flow situation to the free flight case. The correction methods addresses e.g. Mach number and incidence corrections and wall and model support interference. Comprehensive information on correction methods is given in the AGARDographs 109 and 336 on "Wind Tunnel Wall Corrections" [1], [2] and AGARD-CP-535 [3]. Closed test section wall interference is also compensated by adjustable or slotted walls, thus diminishing wall induced pressure gradients and streamline curvatures.

Measurement techniques and application examples discussed in the following are related to aircraft model testing in Göttingen-type low-speed, subsonic and transonic wind tunnels.

2.2 Vortex Flow Physics Aspects

Here, the application scenarios of the experimental methods addressed are related to separated flow with the evolution and development of large-scale vortices. Aerodynamic forces and moments, surface pressures, velocity fields and surface flow visualization is of interest to evaluate the aerodynamic characteristics and to analyze the underlying flow physics effects. As the vortical flow is per se of unsteady nature also for steady free stream conditions time-resolved measurements provide important insight on instability mechanisms and unsteady aerodynamic loading. Measurements of high spatial resolution are highly desired to analyze small-scale structures of the separating and rolling up shear layers and inner core structures of large-scale vortices.

The first scenario is the well-known *leading-edge vortex development* present at low aspect ratio wings of moderate to high wing sweep [7]. Leading-edge vortices (primary vortices) evolve even at low angles of attack inducing further surface flow separation in form of secondary vortices. The separation line of the

secondary vortices is located outboard of the trace of the primary vortex suction peak in the region of the adverse pressure gradient acting on the surface flow directed to the leading-edge. The secondary vortex associated with a turbulent boundary layer separation is located closer to the leading edge in comparison to a secondary vortex developing from laminar boundary layer separation. Also for the primary vortex development, it is important if the separating shear layer is linked to a turbulent or laminar boundary layer separation where the boundary layer state of both the wing upper (suction) and lower (pressure) side has to be taken into account. A large number of investigations are devoted to this flow type. Depending on the objective fundamental flow physics issues but also application aspects are in the foreground. There is an extensive database for the flow on slender, highly swept wings with sharp leading edges [20]. The influence of laminar or turbulent boundary layers on the formation of primary and secondary vortices has been documented, and Reynolds and Mach number effects have been investigated [25]. In the case of round leading edges, the topology of the vortex flow is determined by the not geometrically fixed position of the primary separation line, which is determined by the prevailing flow conditions and boundary layer development. In addition, at high angles of attack, a structural change in the leading edge vortices occurs, depending on leading edge sweep and angle of attack, which manifests itself in a transition from a partial or fully developed (stable) to a burst (unstable) vortex core flow [7]. The transient flow field with inherent instability mechanisms downstream of the vortex bursting location requires time-accurate measurements. For full aircraft configurations, the above-mentioned flow phenomena occur in a superimposed form, resulting in a very complex flow field [6]. A correct reproduction of the domains of vortex-dominated and separated flow within a numerical simulation depends crucially on the particular turbulence modelling used and its conditioning [16]. At configurations of moderate leading edge sweep (about φ_w = 45°–55°) and round leading edges, vortex systems form in the medium angle of attack range (about α = 8°–16°) the separation of which only extends over a rearward part of the leading edge. Towards the apex there is attached flow. Due to the moderate leading edge sweep, the partially developed vortices usually burst over the wing. With a round leading edge, a strong Reynolds number sensitivity occurs. Depending on the geometry, in addition to the actual leading-edge vortex (main vortex), a further leading-edge vortex may develop upstream evolving from a laminar bubble-type separation. Figure 16-1 shows the different stages of leading-edge vortex evolution depending on wing sweep and angle of attack for subsonic, shock-free conditions. Consequently, one can distinguish between partially developed, fully developed, spanwise fixed and burst leading-edge vortices. All these development stages have to be considered when conducting flow field measurements. For the high subsonic and transonic region vortex-shock interactions have to be taken into account as well.

The second scenario is the development of the *wake vortex system* due to the roll-up of the vortex sheet shed at the wing trailing-edge linked to the wing tip vortex, discussed here for transport-type aircraft, Fig. 16-2. Wake vortices develop due to the lift an aircraft produce to fly [8], [22]. Generating lift, the pressure on the wing lower surface is higher than the pressure on the wing upper surface. Thus, air flows around the wing tip from the lower to the upper surface resulting in a strong vortex, the so-called “wing tip vortex”. Further, the fluid coming from the wing upper and lower surfaces exhibit a different sense of direction at the wing trailing-edge. Therefore, a free shear layer or vortex sheet develops, which is connected with the respective wing tip vortex in the span direction. This free shear layer rolls up due to it’s self-induction together with the wing tip vortex into a single rolled-up vortex for the left and right wings, respectively. Consequently, two counter-rotating trailing vortices exist, which can exhibit cross flow velocities of up to 100 m/s in their core region depending upon flight conditions and airplane size. Those trailing vortices remain downstream up to hundred wing spans and more, before they decay due to instability mechanisms and/or due to atmospheric effects. The strength of the two trailing vortices, which remains after the roll-up process, is proportional to the total circulation and thus to the lift, which compensates the aircraft weight. The safety margins for the longitudinal distance between two airliners depend therefore on their maximum take-off weight. Also for military aircraft, wake vortices are of particular interest because their impact can lead to considerably high structural dynamic loads [21]. Thereby, the formation flight, the approximation to a tanker aircraft for air refueling or flying through the wake of the opposing aircraft during air combat are of special interest. Considering the downstream development, a vortex wake can be divided into four regions: (i) The near field, within a distance of about 0.5 wing spans, which is characterized by the formation of highly concentrated

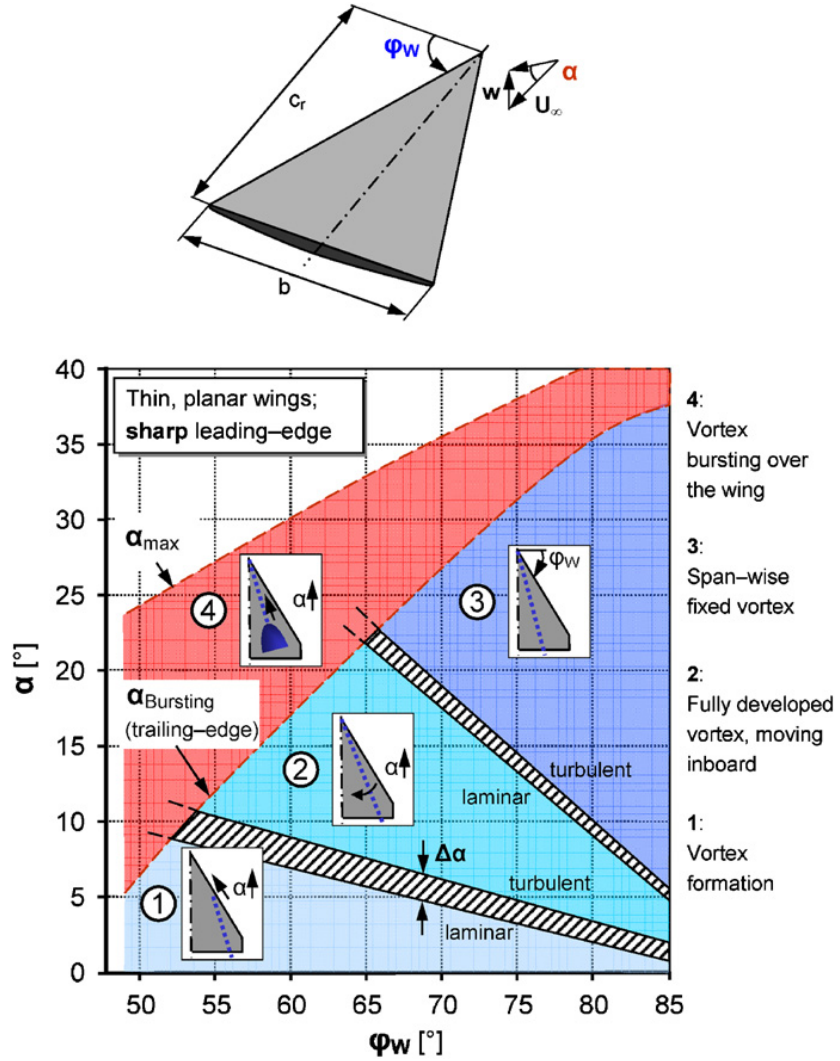

Figure 16-1: Delta wing vortex flow stages as function of wing sweep φ_W and angle of attack α, [7].

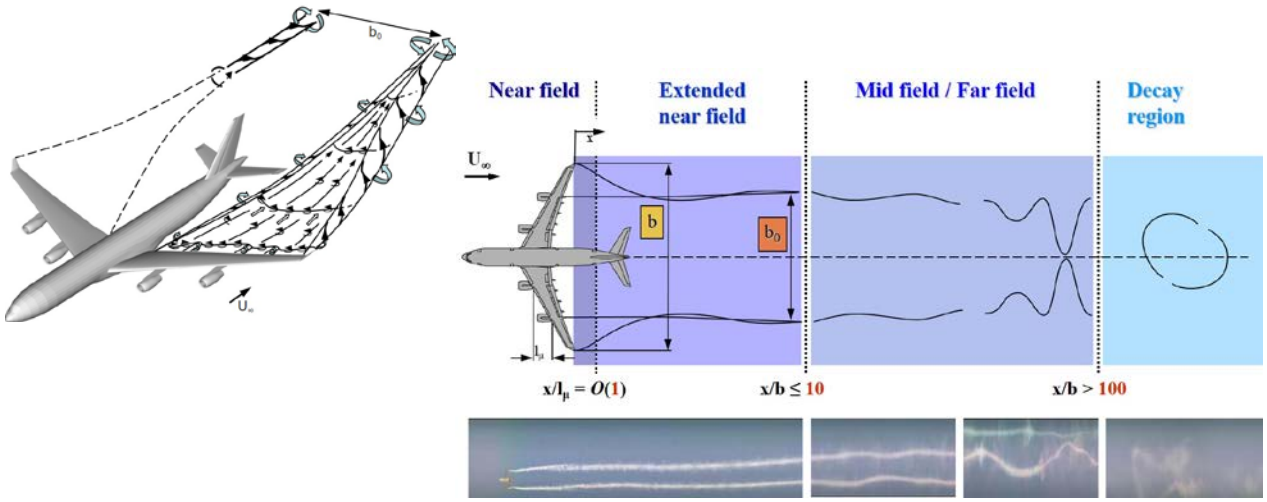

Figure 16-2: Wake vortex evolution and roll-up process and stages of wake vortex life span; b: wing span, b_0: lateral distance of the two rolled-up wake vortices, [8].

vortices shed at all surface discontinuities. (ii) The extended near field, related to a distance within 0.5 to 10 wing span dimensions, where the wake roll-up process takes place and the merging of dominant vortices (e.g. shed at flap edge, wing tip, etc.) leads gradually to two counter-rotating vortices. (iii) The mid and far field, covering a range from 10 to 100 wing span dimensions, where the wake is descending in the atmosphere and linear instabilities emerge. (iv) The dispersion region, with a distance larger than 100 wing span dimensions, where fully developed instabilities cause a strong interaction between the two vortices until they collapse.

These two vortex flow scenarios constitute two typical examples of complex separated flow at wings of small and large aspect ratio to highlight flow patterns featuring a broad range of spatial and temporal scales.

2.0 EXPERIMENTAL TECHNIQUES

An overview of model installation in the wind tunnel test section and standard wind tunnel measurement equipment to obtain aerodynamic quantities can be taken from Figures 16-3 and 16-4. The equipment includes balances, pressure sensors, probes for flow field velocity and pressure measurements and optical systems to derive surface flow information, pressure and velocity fields. A comprehensive overview on methods in experimental fluid mechanics is also given in [32].

2.1 Forces and Moments

Forces and moments are measured with external or internal balances consisting of up to six components, i.e. load cells or strain gauge arrangements, respectively, to determine drag, side and lift forces and rolling, pitching and yawing moments. Consequently, balance measurements are carried out to obtain the integral aerodynamic loads acting on the model employed for the analysis of aerodynamic performance and flight mechanics stability and control properties. Loads due to the mass of the model with respect to inertia and gravity are measured within a tare run for wind-off conditions (“static calibration”). These loads are subtracted from the overall loads under wind-on conditions to obtain the aerodynamic loads.

External balances are located outside of the wind tunnel model. They can be attached to the model sting/ or support system, respectively, or placed as an underfloor, side wall or top wall installation. Concentrating on the aerodynamic loads acting on the model, the load bearing elements outside the model have to be shielded from the free stream impact, e.g. by covers, to avoid flow induced loads on these components. Alternatively, a “dynamic calibration” may be performed with a detachment of the model from the load bearing system to obtain the flow induced loads on the sting/support system only. The model is to be kept in place by additional holders to maintain the interference of the model on the sting/support flow situation. The flow induced loads on the sting/support system can then be subtracted from the total aerodynamic loads acting on model and support. An internal balance is directly integrated in the model. Thus, neither shielding of model sting components is necessary nor flow induced loads on sting components have to be determined. A six-component internal strain-gauge balance is shown in Figure 16-4. For every measured data point, e.g. with respect to angle of attack, sideslip and roll angle, and further variations, e.g. due to control surface settings, the forces and moments are obtained with a certain sampling rate over a certain time period. Consequently, time-averaged quantities and time-resolved data may be available. Focusing e.g. an angle-of-attack polars, pitch pause or continuous sweep measurements are usually performed. An accuracy in the order of one drag count, $\Delta C_D = \pm 0.0001$, is a typical standard.

2.2 Surface Pressures

Steady and unsteady surface pressure distributions are experimentally obtained using distributed pressure tabs over the surface or applying the Pressure Sensitive Paint (PSP) method.

- Generic models
- Transport aircraft
- Fighter aircraft
- Unconventional A/C, UAVs, Helicopter

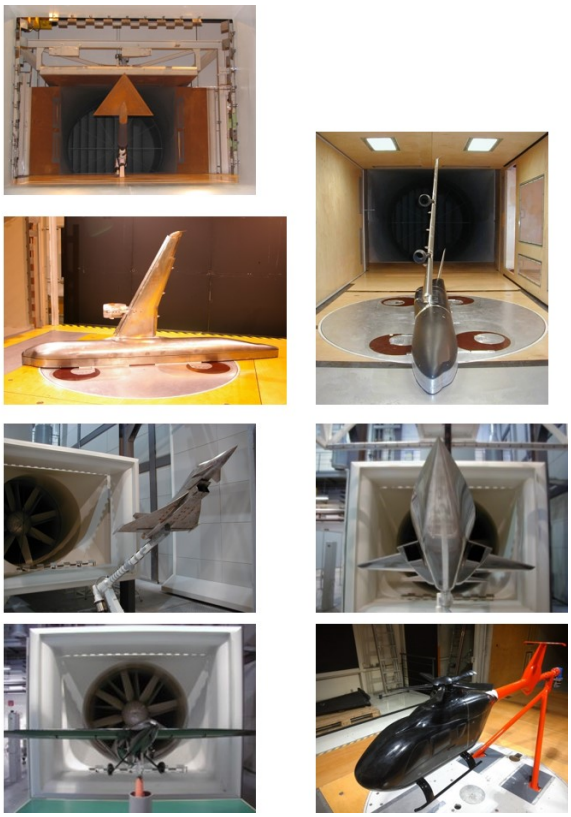

Figure 16-3: Versions of wind tunnel models (full, half-span) and test section installations.

- Forces and Moments
  - **External** six-component (underfloor) balances
  - **Internal** six-component strain gauge balances
- Surface Pressures
  - **Steady** pressure distribution (multi-channel scanner)
  - **Unsteady** pressures (multi-channel system)
- Velocity and Pressure Fields
  - **Hot-wire anemometry**
  - Particle Image Velocimetry **(Stereo-PIV)**
  - Multi-hole pressure probes
- Visualization
  - Laser light sheet
  - Oil flow visualization
  - Liquid crystal technique

Figure 16-4: Examples of measurement equipment and testing applications.

2.2.1 Pressure Tabs

The classical approach for the measurement of surface pressure distributions is to use pressure tabs taking static pressure values at a number of discrete points over the surface. For a sufficient number of pressure tabs, pressure based loads can be obtained by integration over the whole surface or parts of the surface. Pressure transducers, taking also time-accurate values, can be placed very close to the surface or even flush mounted. When using hundreds of pressure tabs there may be space problems for installing the sensors close to the surface or cost reasons may exclude such a solution. Therefore, holes are drilled in the surface connecting these holes with tubes to a (multi-channel) pressure scanner module located inside or outside the wind tunnel model. The pressure levels of the connected tubes are then sequentially scanned with high repetition for a certain time period to derive averaged quantities. There are certain requirements on the drilling of the pressure orifices. The axis of the hole should be in line with the surface normal. The orifice must be free or ridges or other geometric disturbances. The diameter of such orifices is usually about 0.3 mm. Modern model production methods like 3D printing or additive manufacturing, respectively, open up possibilities to integrate orifices and tubes directly in the model structure at positions, e.g. very close to the leading-edge or at deployed slats, where such a placing is not possible with classical drilling processes.

Focusing on unsteady surface pressure measurements, the corresponding transducers have to be located directly at the surface to avoid installation effects on the temporal characteristics of the measured pressure signal. Consequently, miniature unsteady pressure transducers, often of piezo-resistive type, are embedded at certain positions in the model surface. Contrary, when placing the sensors downstream of cavities or tubes the acoustic properties of this installation have to be considered. A frequency dependent calibration for each tube or cavity arrangement is necessary accounting for the deviations in amplitude and phase between the pressure fluctuations present at the surface orifice and the one measured by the sensor attached to a cavity or tube to reconstruct the unsteady characteristics with a certain level of accuracy.

2.2.2 Pressure Sensitive Paint

The Pressure Sensitive Paint (PSP) technique is an optical measurement method to conduct pressure measurements on surfaces without affecting the surface of the model by drilling holes [23], [33]. The model surfaces are coated with a special paint using a spray gun. The painted surface is then illuminated for example by UV light. The intensity of the resulting fluorescence light depends on the local oxygen concentration and allows for the determination of the areal pressure distribution. Generally, the PSP technique is based on an oxygen quenching process in which photo-chemical molecules excited by light are deactivated by collisions with oxygen molecules in spite of irradiation of fluorescence light. This leads to different degrees of luminosity on the surface of the model depending on the local pressure. A final pressure map is obtained from images applying Charge Coupled Device (CCD) cameras using complex image processing techniques. Pressure data taken from very few “reference” tabs are usually employed for a precise adjustment of the PSP derived pressure levels. The PSP methodology can be applied for low speed up to hypersonic test conditions. Often, the sensitivity is optimized in the pressure range of 0.1 – 1.5 bar which is a typical pressure range for transonic flow conditions. Under quasi-static conditions a resolution of around ±1.5 mbar with a response time of 0.5 s could be achieved. Low speed conditions needs special coating developments due to the relative low pressure difference affecting the local oxygen concentration. Further, unsteady PSP, so called iPSP, to capture surface pressure fluctuations has been introduced and successfully applied on a variety of wind tunnel applications [33].

As discussed in Sec. 2.2.1, conventional pressure measuring is only capable to take surface pressures at discrete points by installing pressure sensors such as taps and transducers, whereas the areal PSP method enables a measurement of the entire surface. The location of pressure taps must be determined prior to model manufacturing excluding any re-arrangement later on. Further, there are restrictions to drill holes in thin parts of wind tunnel models, whereas wall thickness is not a matter applying the PSP coating to the model surface.

2.3 Flow Field Velocities and Pressures

Velocity and pressure distributions related to the flow field around the model can be detected using intrusive and non-intrusive techniques. Probe based measurements are of intrusive type introducing possible disturbances to the flow field development. Therefore, specific knowledge and experience is needed to apply such methods on flow field scenarios associated with separated and vortical flows. The most prominent non-intrusive technique is Particle Image Velocimetry (PIV) to acquire velocity components in all three spatial directions while Laser Doppler Anemometry (LDA) loses importance due to the continuously increasing capabilities of PIV with respect to spatial and temporal resolution.

2.3.1 Probe Based Measurements

Velocity data with respect to high temporal resolution (up to 20 kHz) can be gained from Hot Wire Anemometry (HWA) [9]. Probes feature single-wire and multi-wire sensor arrangements the employment of which depends on the application scenario and flow field characteristics [24]. The sensors consist of 5 µm diameter platinum-plated tungsten wires giving a length/diameter ratio of about 250. The measuring volume is approximately 0.5 up to 1 mm^3. For example, tripel-wire probes enable the measurement of time-dependent velocities in all three spatial directions. The spatial unambiguous range of a triple-wire probe is typically restricted to an angle range of ±35 deg. A cross-wire probe, with the sensors orientated perpendicular to each other, exhibits an increased usable angle range of ±45 deg. Velocity vectors related to larger flow angles can not be correctly determined by such wire arrangements. The use of a cross-wire configuration generally assumes a known flow direction with which the probe most be aligned. The nature of vortex-dominated flow precludes any knowledge on the direction of the velocity vector. For the axial component it is often assumed to point e.g. in positive x-direction. In order to determine all three velocity components the cross-wire probe has to be rotated and at least two traverse sweeps are necessary to obtain the streamwise (u), lateral (v) and vertical (w) velocity components. This procedure can be avoided when using a four-wire probe consisting of a combination of two cross-wire probes oriented 90 deg to each other. Besides standard type probes there is a variety of customized probes. The unambiguous angle range can be enlarged, e.g. up to ±120 deg, by introducing additional wires, e.g. two pairs of heating and sensing wires to provide information on the main flow direction added to a four-wire probe.

Hot wire probes are mostly operated with a constant-temperature anemometer system. Signal conditioner modules transform the bridge output voltages into a suitable range for multi-channel A/D converters of the data acquisition systems. Further signal conditioning with respect to offset compensation and analog low-pass filtering is applied. An additional temperature probe is used to correct the anemometer output-voltages if ambient flow temperature varies. To calibrate the hot-wire probes computer-aided fully automated procedures have been developed measuring the anemometer output voltages for a range of prescribed velocity values and orientations of the probe relative to the free stream velocity vector, i.e. angles of incidence and yaw or inclination and azimuth, respectively. Using this technique actual flow conditions, i.e. varying flow angle and velocity magnitude are considered during the calibration procedure. It accounts also for the interference between prongs and wires and the wires themselves, manufacturing inaccuracy and divergence from an ideal probe geometry, and within a certain time interval, for the different soiling of the single wires. For this direct calibration method there is no need of simplifying assumptions concerning the sensor characteristics or about physical laws governing the sensor cooling and no yaw or pitch angle factors have to be introduced. The calibration grid itself is too course to determine the magnitudes and the associated directions of the measured velocity vector exactly. Therefore, the calibration grid is processed to a highly refined grid called look-up table. For the generation of look-np tables several numerical methods are implemented. The calculation of the instantaneous velocity vector is done for each value of the stored time series of anemometer output voltages. A search algorithm is used to determine the closest look-up table voltages relevant to the measured voltages. The velocity magnitude and the associated flow direction are then calculated by interpolation between the voltages of the measurement conditions and the adjacent look-up table data set.

Regarding pressure fields, multi-hole probes, mostly five-hole or seven-hole probes, are used to determine total pressure, static pressure and velocity components based on pressure differences due to the arrangement of the holes [15]. Minimum probe head sizes may be around 2 mm. Usable angle ranges are from ±40 deg up to ±60 deg. A calibration procedure with respect to velocity and flow angle variation is conducted like it is the case for hot-wire probes. Measuring unsteady quantities, unsteady pressure transducers have to be integrated in the probe head. Placing the transducers in the probe shaft or outside the probe will result in channels and tubes acting as an acoustic system with respect to amplitude and frequency characteristics. This arrangement needs a frequency dependent calibration as addressed in Sec. 2.2.1. Newest developments concentrate on fibre optic sensors avoiding such calibrations.

2.3.2 Particle Image Velocimetry

Particle Image Velocimetry (PIV) is an optical based measurement technique which is state-of-the-art for acquiring non-intrusive velocity field data [19], [23]. Small tracer particles advected by the flow are illuminated twice by very short pulses of a laser light sheet defining the measurement plane. Digital optical sensors capture the light scattered by the particles. Instantaneous velocity vector fields can be obtained in high spatial and temporal resolution employing image analysis techniques. The principle of the PIV measurement technique relies on the physical definition of velocity as a differential quotient. The trajectory of many tracer particles following freely the flow can be captured with CCD- or (Complimentary Metal-Oxide Semiconductor) CMOS cameras by illuminating a plane in the flow with two very short light pulses (few nanoseconds) within a time difference of a few microseconds. The two particle images captured at two defined time instants are stored on two frames of the CCD or CMOS sensor. This allows to cross correlate the two particle image distributions in small interrogation areas in order to determine their displacement on many positions of the observation field locally. Using the image magnification factor this method enables the measurement of typically more than 10,000 instantaneous velocity vectors for each double-image of the tracer particles inside the light sheet plane. Extending the PIV system to a stereoscopic camera set-up (Stereo-PIV) it is possible to determine not only the in-plane velocity vectors but also the velocity component normal to the light sheet. Thus, all three velocity components related to the flow field of the measurement plane are surveyed. PIV is used for microscale as well as for large scale applications and in flows with velocities between a few mm/s and up to a km/sec.

Tomographic (Tomo) PIV can be seen as an extension of the Stereo-PIV concept and enables the instantaneous measurement of all three velocity components in a complete 3D measurement volume [14]. Tomo-PIV systems use the same laser and camera equipment as in planar PIV setups, i.e. a direct migration from 2D- or Stereo-PIV to Tomo-PIV is straightforward adding two or more cameras. Tomo-PIV is based on the principle of tomographic reconstruction of voxel intensities in a volume that is well known from Computed Tomography (CT) in medical imaging. For an accurate voxel reconstruction all cameras must be mapped in space into the same coordinate system with an accuracy of better than 0.1 pixel. This highly accurate camera calibration is realized using volume self-calibration methods. Three-dimensional velocity vector maps from two 3D particle images are computed applying an iterative three-dimensional cross-correlation technique using deformed interrogation volumes. The PIV technique provides a highly reliable basis of experimental flow field data for direct comparison with results of high fidelity computational fluid dynamics simulations constituting validation data to further develop and improve numerical flow modeling.

2.4 Surface Flow Quantities

Surface flow characteristics can be obtained from surface flow visualization which is often of oil flow type [32]. Quantitative information can be derived from shear stress sensitive liquid crystal coatings following a specific calibration [28], [31].

Shear-stress-sensitive/temperature-insensitive liquid crystal coatings have been used in order to investigate unsteady flow physics associated with vortex-dominated flows. The liquid crystal technique has been

demonstrated as an effective “flow-visualization” tool for flight and wind-tunnel testing over the whole Mach number range from low speed to hypersonic. A thin coating of liquid crystals applied to a surface scatters white light in such a manner that specific wave lenghts are emitted in certain directions. The coating responds to changes in surface shear stress by altering the scattering angle for each wavelength, or color. Any abrupt change in shear stress such as through boundary-layer transition or vortex-induced change in near-wall velocity gradients produces a clear change in the color seen at a fixed observation point. The liquid crystals do not become saturated at a particular condition, so many different test conditions can be studied with one application. The response time of the liquid crystal coating was documented to be equal to, or less, the time interval between sequential frames recorded at 1 kHz, i.e. 1 ms. Metal surfaces of models are primed with a suitable black background paint to avoid specular reflections. Under normal illumination, any surface point exposed to a shear vector directed away from the observer exhibits a color change, with the color shift being a function of shear magnitude and direction relative to that observer. Conversely, if the shear vector is directed towards the observer, the coating exhibits no color change and appears as a rust or brown color, independent of shear magnitude and direction. The limitations of this technique are due to the requirement of multiple viewing angles and the fact that the color change is a function of both skin friction and direction of observation. Variations in light direction and intensity have to be checked to get optimum and comparable record conditions. Further, lighting and viewing angles must be selected to avoid specular reflection or glare. CCD or CMOS cameras are employed to record the changes in surface color.

Further sensor developments for the measurement of surface pressure and shear stress have been investigated in lab experiments. The so called Shear and Stress Sensitive Film (S3F) sensor is based on the 3D deformation of an elastic, incompressible film [11]. This sensor layout does not depend on oxygen quenching and thus can work in most fluids. It acts as a differential pressure gauge. The sensitivity can be tuned to match the test flow conditions. It is sensitive to both shear and pressure components. Measurements of pressure and skin friction in several low-speed environments have been demonstrated and the data compare favourably with results of standard measurement techniques. The inherent difficulty is due to the embedding of the elastic film in the model surface structure.

2.5 Transition Detection

Infrared thermography has been established as a valuable investigation tool for experimental aerodyna-mics, especially for transition detection [13]. The use of infrared (IR) cameras has been proven to be effective to identify both the difference in recovery temperature and the difference in heat transfer rate between the laminar and turbulent regions of a boundary layer. This task, however, remains challenging when considering complex models made of non-uniform material and wall thicknesses, in particular, in low-speed wind-tunnel experiments. Post processing methods are used for the automatic detection of transition start and transition end on complex wind-tunnel models based on thermography with uncooled infrared cameras. They are effective in detecting the transition location by comparing two successive thermograms shortly after the transition region reached its final location. It is an extension of the known thermogram subtraction method employed for high-speed experiments. Its virtue is that it is sufficient to preheat the model externally before the wind-tunnel startup, making internal heating devices obsolete. This simplifies the experiments and allows the application to models where an integrated heating device is not feasible.

2.6 Surface Deformation

Deformations and deflections occurring on wind tunnel model geometries under aerodynamic loads can be determined by stereo photogrammetry measurement techniques [5]. Digital cameras record certain marker arrangements put on the surface. The markers can be part of the surface or virtually placed via a superimposed shadow image. The Direct Linear Transformation (DLT) method is used to reconstruct the three-dimensional coordinates of the markers, placed e.g. on the wing surfaces, from the pixel coordinates in the image planes. A calibration target consisting of a known grid of markers is used to obtain an array of reference points uniformly distributed in the measurement volume. This reference information is employed

to compute the DLT parameters for the cameras involved. Reconstructing the position of the reference points in the object space using the transformation parameters obtained during the calibration indicate an average measurement uncertainty which may be in the order of 0.01 mm depending of the components involved.

3 VORTICAL FLOW ANALYSIS – DELTA, DIAMOND AND LAMBDA WING

Generally, global and local data of sufficient spatial and temporal resolution comprising aerodynamic forces and moments, surface pressures and quantities of the surrounding and near wall flow area are required to set up a sound data base characterizing aerodynamics and flow physics properties. Examples are presented for bursting of strong leading-edge vortices, evolution of dual leading-edge vortices, incipient separation at blunt leading edges, and motion induced unsteady aerodynamics at transonic speed.

3.1 Delta Wing Flow Features

Delta wing research activities often focus on a sharp leading-edge because primary separation is fixed and the leading–edge vortex development is only less influenced by Reynolds number effects. A blunt leading-edge complicates the vortex aerodynamics as the position of the separation line is free to move around the leading-edge determined by the pressure gradient and the boundary layer development. Thus, leading-edge radius, angle of attack, Reynolds number and Mach number are the main parameters determining the onset of vortex evolution as well as position and strength of the primary vortex. For the sharp leading-edge case, angle of attack and Mach number are the main parameters.

3.1.1 Sharp Leading-Edge – Vortex Bursting

Regarding the well-known leading-edge vortex flow scenario, cf. Fig. 16-1, some important features of the vortex breakdown flow can be derived by analyzing fluctuation intensities along with spectral quantities of cross flow velocities together with surface pressures [7]. Here, results of turbulence intensities of axial velocity and surface pressure fluctuations are shown for a 76 deg swept, sharp-edged delta wing ($\Lambda = 1$) at high angle of attack. The Reynolds number based on the mean aerodynamic chord is $Re_{mac} = 1.07 \times 10^6$ and the Mach number is Ma = 0.11. The time-dependent velocities and surface pressures have been obtained using classical measurement techniques, namely hot-wire anemometry employing multi-wire probes and unsteady pressure transducers embedded in the wing surface.

For an angle of attack of $\alpha = 35$ deg, vortex bursting takes place at a relative wing root location of $x/c_r = 0.49$, with c_r is the root chord length, Fig. 16-5. The flow pattern of the vortex core is significantly changed in comparison to the non-burst stage. Next to the original jet–like core a region of strong flow deceleration occurs. This region of retarded axial core flow is caused by the adverse pressure gradient arising at high angle of attack. The corresponding strong velocity gradients and the rapid change from jet–like to wake–like core flow evokes an overall maximum in turbulence intensity at the vortex center. Downstream, the region of maximum turbulence intensity expands rapidly which is evident at 90% wing root chord. The associated local turbulence maxima are located in a limited radial range around the burst vortex core. This area corresponds to the points of inflection in the radial profiles of the retarded axial core flow. Analyzing the spectral content of the velocity fluctuations it is shown that the breakdown flow exhibits a significant spectral peak indicating that turbulent kinetic energy is channeled into a narrow band. The frequency related to this spectral peak is named “dominant frequency”. This frequency dependent energy concentration is linked to a specific instability mechanism called helical mode instability of the breakdown flow [7]. Hence, quasi–periodic aerodynamic loads result which may strongly excite structural modes.

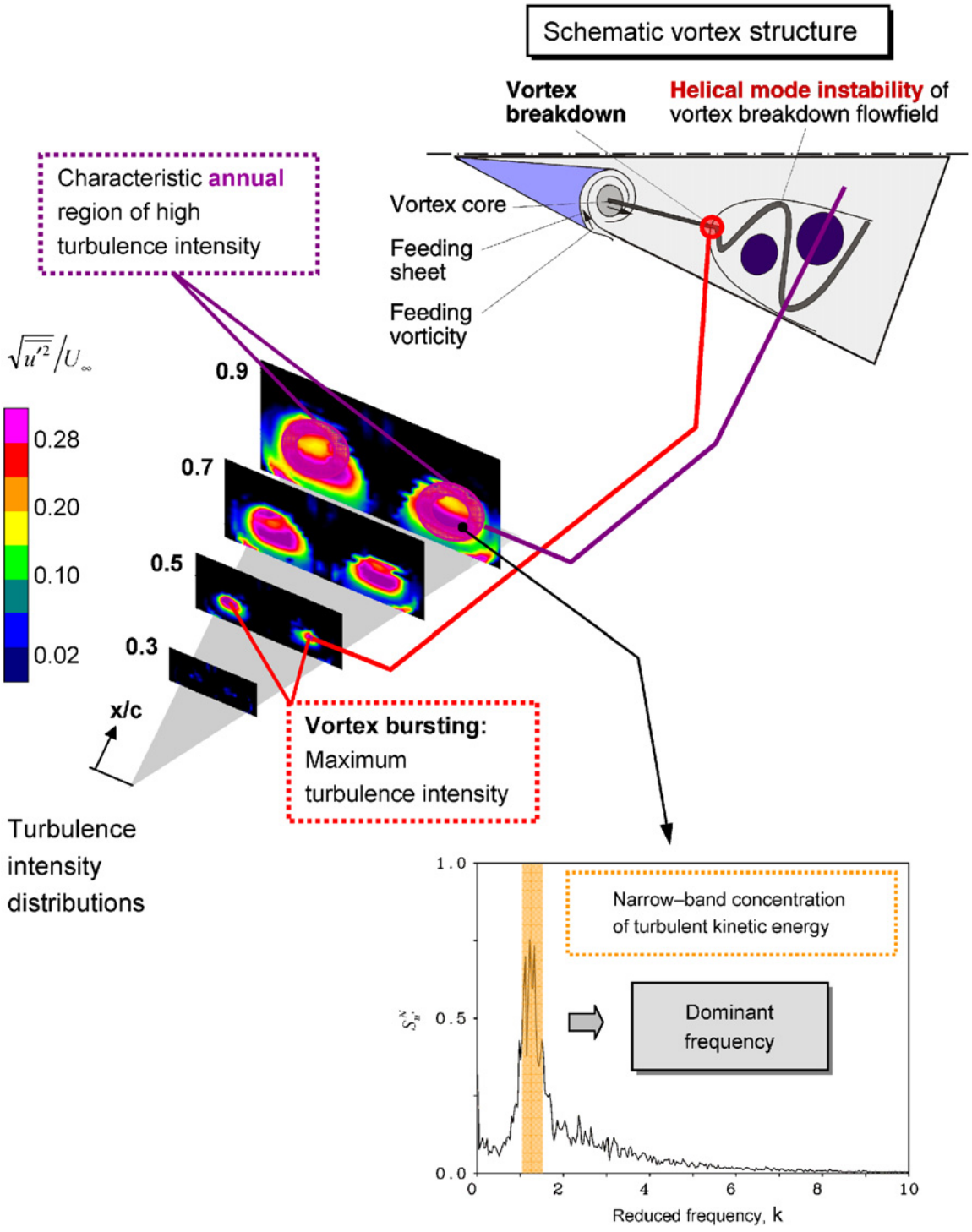

Figure 16-5: Characteristic delta wing turbulence intensity distributions and power spectral densities of velocity fluctuations for the leading-edge vortex breakdown flow field; φ_W = 76 deg, α = 35 deg, Re_{mac} = 1.07 x 10^6, Ma = 0.11; [7].

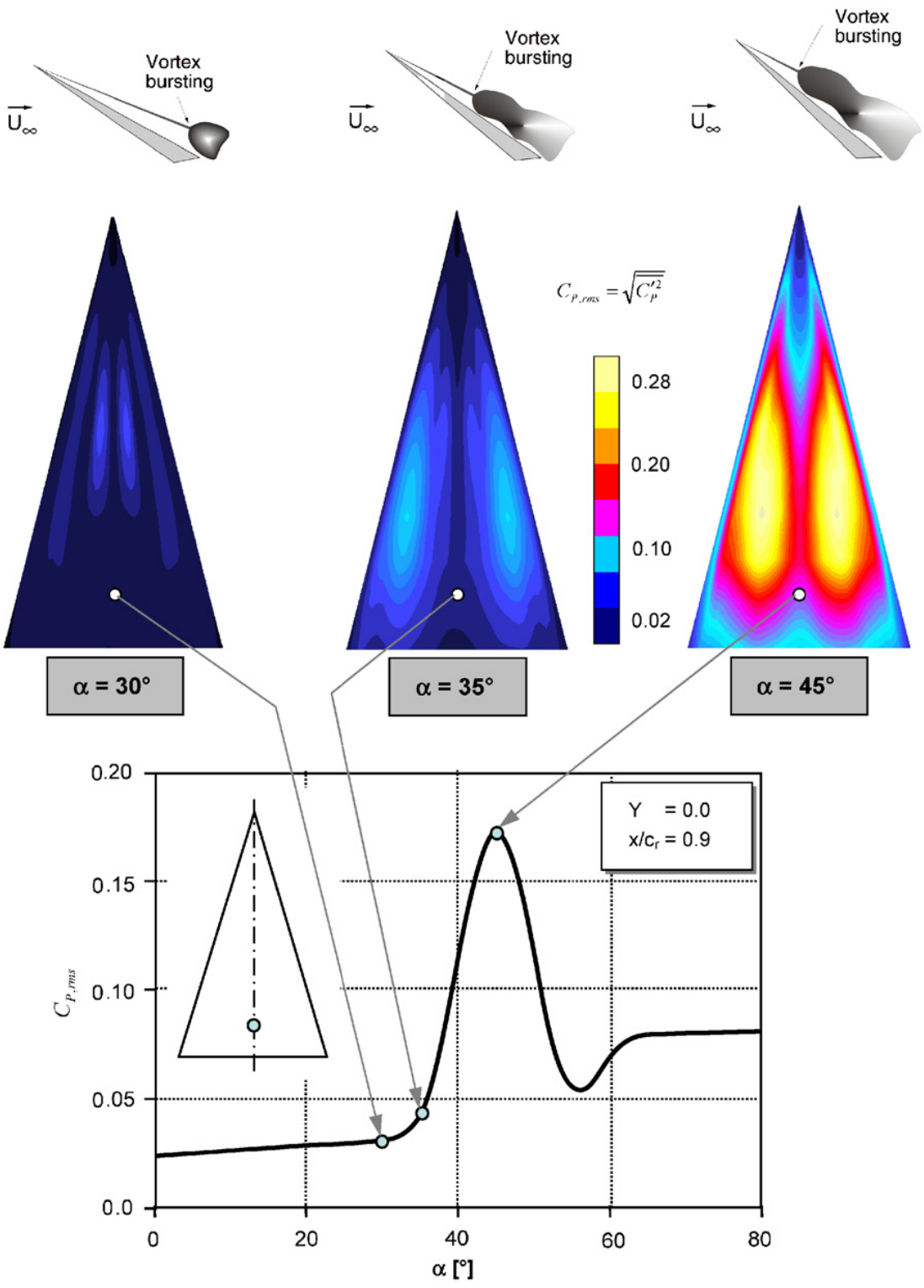

Figure 16-6: Delta wing rms pressures as function of angle of attack considering especially cases of leading-edge vortex bursting over the wing; φ_W = 76°, Re_{mac} = 1.07 x 10^6, Ma = 0.11; [7].

The impingement of burst leading–edge vortices is a source of buffet excitation on an aircraft experienced on the wing surface or on other surfaces such as the fin. The buffet excitation is substantiated by the corresponding surface pressure fluctuations, Fig. 16-6. The rms pressures are plotted as a function of angle of attack for the symmetry location at 90% wing root chord. In addition, patterns of rms surface pressures are shown for α = 35, 40, and 45 deg. If vortex breakdown takes place in the rear part of the wing the rms surface pressure distribution is less affected. With the breakdown position moving upstream the pressure fluctuation intensities increase strongly, especially beneath the vortex axis, where the distance to the region of maximum flow field turbulence is the smallest. The main impact exists at α = 45 deg when the surface pressure fluctuations reach an absolute maximum with rms levels above 30%. A further increase in angle of attack shifts the breakdown position closer to the apex and the rms pressures decrease. This decrease is due to the detachment of the vortex axis reducing the impingement of the highly fluctuating flow field on the wing surface. Consequently, analyzing such flow scenarios requires time-accurate measurements of sufficient spatial resolution for both the flow field and the surface related quantities.

3.1.2 Round Leading-Edge – Main and Inboard Leading-Edge Vortices

A comprehensive test series on delta wing flow features have been conducted on a 65 deg swept delta wing (Λ = 1.865) fitted with sharp and blunt leading-edge. These activities have been coordinated within the Vortex Flow Experiment 2 (VFE-2) activity being part of the Applied Vehicle Technology (AVT) task group AVT-113 “Understanding and Modeling Vortical Flows to Improve the Technology Readiness Level for Military Aircraft” of the NATO Science and Technology Organization (STO) [20], [26], [12]. The experiments taking place from 2003 – 2008 were aimed at an extension of the knowledge on the vortical flow around the configuration with sharp and rounded leading edges. The measurements were accompanied by extensive numerical investigations to support the interpretation of the flow physics [20].

Here, an example is taken for the VFE-2 configuration fitted with the (medium radius) rounded leading-edge at an angle of attack of α = 13 deg. The free stream velocity is U_∞ = 48 m/s resulting in a Reynolds number of 2.0 x 10^6 based on the mean aerodynamic chord and a Mach number of 0.14. The root chord length is c_r = 0.980 m and the wing span is b = 0.914 m. The upstream flow separation takes place in the front one-third of the wing, where the wing is relatively thick, Fig. 16-7. At its very beginning the separated flow region is located close to the wing surface, but further downstream a concentrated inner vortex is formed quite rapidly. Along the blunt leading-edge the curvature radius of the leading-edge remains constant, whereas the local half span increases downstream. This means that the relative leading edge radius becomes smaller towards the trailing-edge of the wing. Hence, the suction at the leading-edge increases downstream, and finally a further flow separation takes place in the downstream portion of the wing, forming the (main) primary vortex there. In the region of the onset of this downstream primary vortex, strong interference with the already existing inner primary vortex takes place. The dominant part of vorticity, shed from the leading-edge, is now fed into the outer primary vortex, whereas the feeding of the inner vortex with vorticity is reduced. Therefore, the inner primary vortex decays downstream due to dominating viscous effects.

The vortex formation strongly depends on the Reynolds number. With decreasing Reynolds number the onset of the outer primary vortex moves upstream and its strength increases, whereas the inner primary vortex is weakened and its position moves distinctly inboard. A reduction in Reynolds number has an analogous effect as an increase in the angle of attack, but nevertheless the reasons for this upstream movement of the onset of the outer primary vortex are different for both cases. With increasing angle of attack the adverse pressure gradients on the upper surface of the wing increase as well, and this leads to the upstream movement of the onset of the outer primary vortex. If the angle of attack is unchanged, however, the adverse pressure gradients remain at the same level, but with decreasing Reynolds number the viscous flow is no longer able to stay attached, and this leads again to an upstream movement of the onset of the outer primary vortex. With decreasing Reynolds number the inner primary vortex is found in a more inboard position. This effect has also been documented by surface oilflow patterns. The topology of the flow field is shown in Figure 16-8 [12]. For distinct locations in the wing mid part, near wall velocity and turbulence

intensity profiles are plotted highlighting boundary layer characteristics. For this relatively low Reynolds number laminar separation and transitional flow physics are affecting the flow in the vicinity of the wing apex. The two primary vortices or dual primary vortex system, respectively, are clearly indicated.

3.2 Diamond Wing Flow Features – Incipient Separation

As discussed in Sec. 3.1.2, blunt leading-edge separation is associated with a complex vortex evolution scenario depending on boundary layer stage and pressure gradients. Consequently, a detailed analysis of the incipient separation flow physics on a medium swept round leading-edge constituted the focus of the STO task group AVT-183 named "Reliable Prediction of Flow Separation Onset and Progression for Air and Sea Vehicles" [27], [16]. In this context, a diamond wing configuration of 53 deg leading-edge sweep with blunt leading-edge contour is considered ($\Lambda = 2.191$). The trailing-edge sweep is −26.5 deg. Over the whole span, the wing has a symmetric airfoil, NACA64A006. This leads to a relative leading-edge radius based on the local wing chord of 0.246% The model root chord is c_r = 1.200 m and the half span is s = 0.657 m. The influence of the test-section boundary layer on the half model flow is reduced by a péniche with a height of 0.090 m.

At low speed wind tunnel conditions, the separation onset of the emerging leading-edge vortex has been studied in detail [10], [16], [17]. The results show that the flow separation onset and the leading-edge vortex evolution are very sensitive to the roughness height and any leading-edge contour modification. Compared to the free transition case [10], both reasonably tripped and over-tripped cases have been investigated [18]. Measurement repeatability issues are reviewed from a short-term and a long-term perspective [18]. As an outcome, a specific leading-edge roughness has been selected for the target flow conditions providing the baseline for complementary high fidelity CFD simulations. Both Stereo Particle Image Velocimetry and Hot-Wire Anemometry are applied to detect the emerging flow phenomena in several chordwise sections including near-wall data. Details of the leading-edge vortex formation and progression are analyzed and discussed. Over almost the entire length of its existence, the leading-edge vortex (LEV) is characterized by retarded axial flow, thus showing vortex bursting tendencies. The corresponding turbulent fluctuations exhibit maxima close to the evolution of the leading-edge vortex and decrease towards the trailing edge. The observed flow separation onset and progression are significant for the AVT-183 diamond wing configuration, and more generally for a moderately swept low aspect ratio wings with rounded leading-edge contour.

The analysis of the AVT-183 configuration with entirely rounded leading edge provides a consistent flow-physical description of the leading-edge vortex formation from a smooth surface separation on boundary-layer level in the incipient separation region, Fig. 16-9a. The vortex confined close to the leading-edge grows with the leading-edge boundary layer and the now weakened leading-edge flow separates and forms the primary vortex [19]. The system's tertiary vortex underneath the primary wing vortex shows a direct connection with the leading-edge confined circulation. As a reaction to the confluent span-wise outboard boundary layer flow from the forward non-separated part of the wing and the inboard flow from the inboard side of the reattachment of the primary vortex the very weak so called displacement vortex is formed. A sketch type summary of the findings is also shown in Figure 16-9b. Here the confluent flow, which produces the so called displacement vortex with the inboard induced flow coming from the primary vortex is shown more clearly. Also the connection of the primary vortex with the smaller vortical region on boundary layer level located close to the edge is depicted together with the evolution of the secondary and tertiary vortices where the primary system lifts off the wing onto the upper surface. The development of this leading-edge confined vortex system is in line with the observation of the "two" primary vortices detected for the VFE-2 blunt leading-edge case.

The example of the AVT-183 diamond wing flow physics analysis highlights that a detailed investigation of smooth surface separation addressing three-dimensional boundary layer characteristics requires a complementary experimental and numerical approach for which data cross comparison is essential.

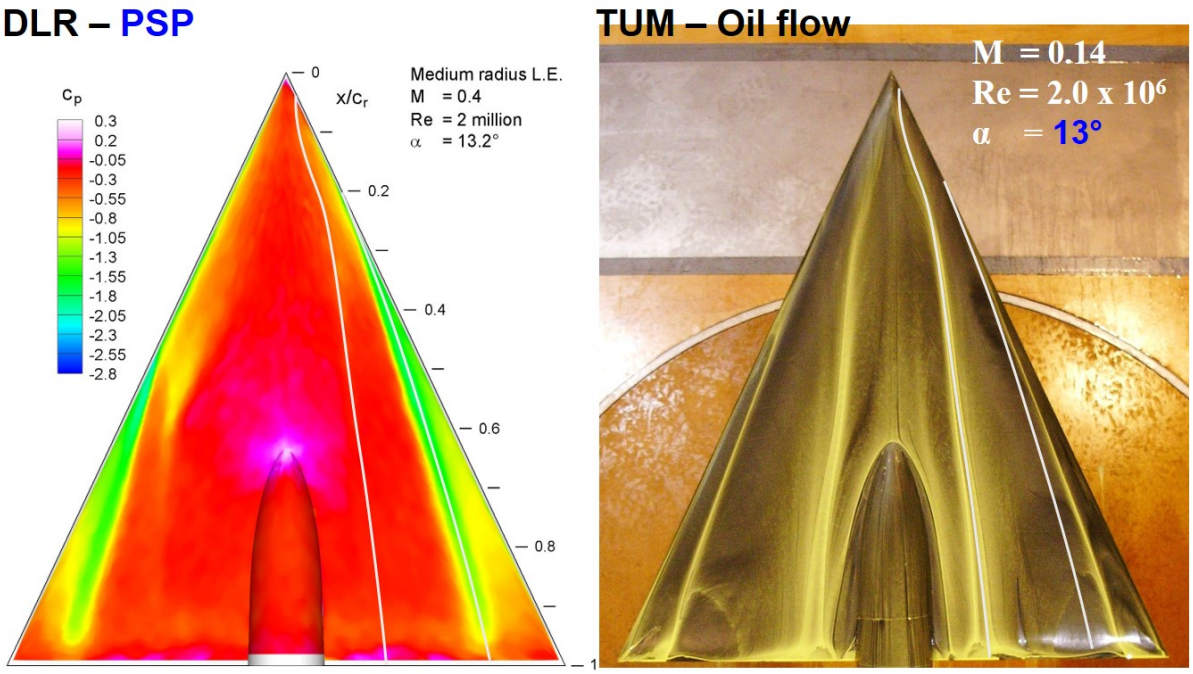

a) Surface pressure distribution, $c_p = (p - p_\infty)/q_\infty$, $q_\infty = (\rho_\infty/2)/U^2_\infty$, based on Pressure Sensitive Paint (PSP) measurements (left) and oil flow pattern of surface flow (right)

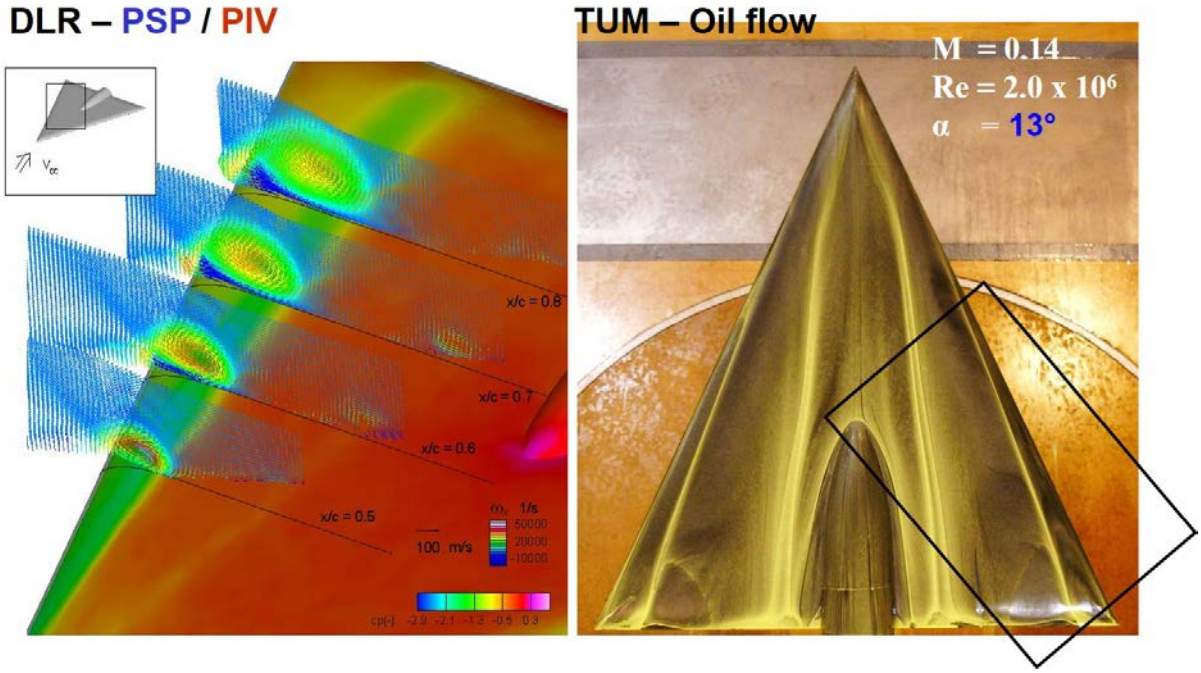

b) Axial vorticity distributions and cross flow velocity vectors based on Stereo Particle Image Velocimetry (PIV) measurements (left) and oil flow pattern of surface flow (right)

Figure 16-7: Delta wing low speed flow characteristics for blunt leading-edge vortex flow separation; φ_W = 65°, α = 13 deg, Re_{mac} = 2.0 x 10^6, Ma = 0.14.

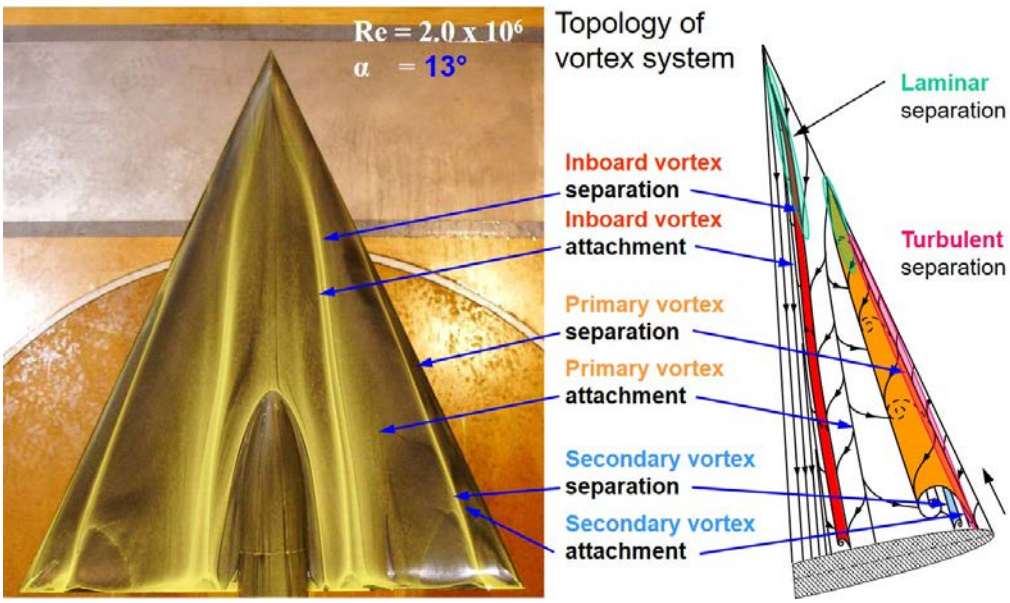

a) Blunt leading-edge separation flow topology based on oil flow pattern

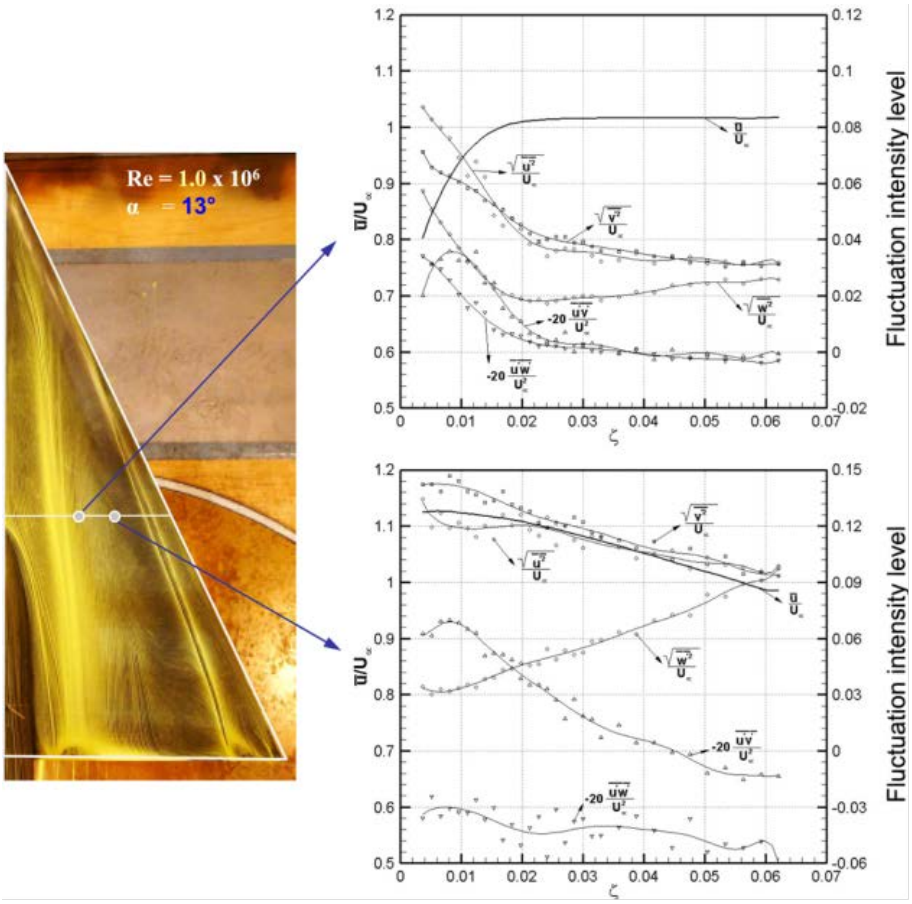

b) Near-wall velocity and turbulence intensity profiles; u', v', w': velocity fluctuations in streamwise, lateral and normal direction; $\zeta = z/(b_l/2)$: normalized wall distance

Figure 16-8: Delta wing near wall flow characteristics for blunt leading-edge vortex flow separation; φ_W = 65°, α = 13 deg, Re_{mac} = 2.0 x 10^6, Ma = 0.14; [12].

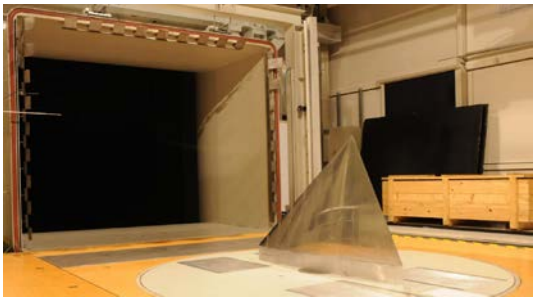

Diamond wing half model configuration installed in wind tunnel test section mounted on six-component underfloor balance with turn table

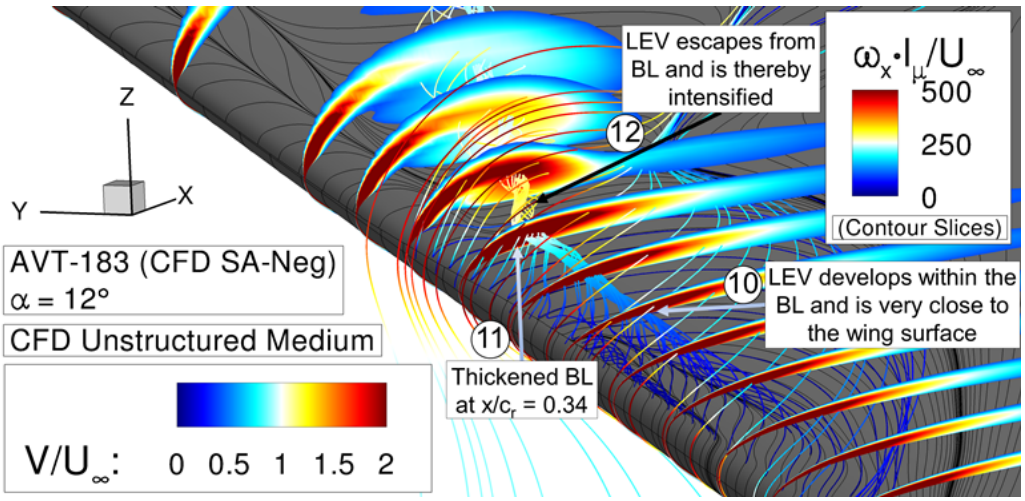

a) Flow separation onset characteristics derived from CFD (URANS) simulations verified by experimental surface pressure and flow field data [17]

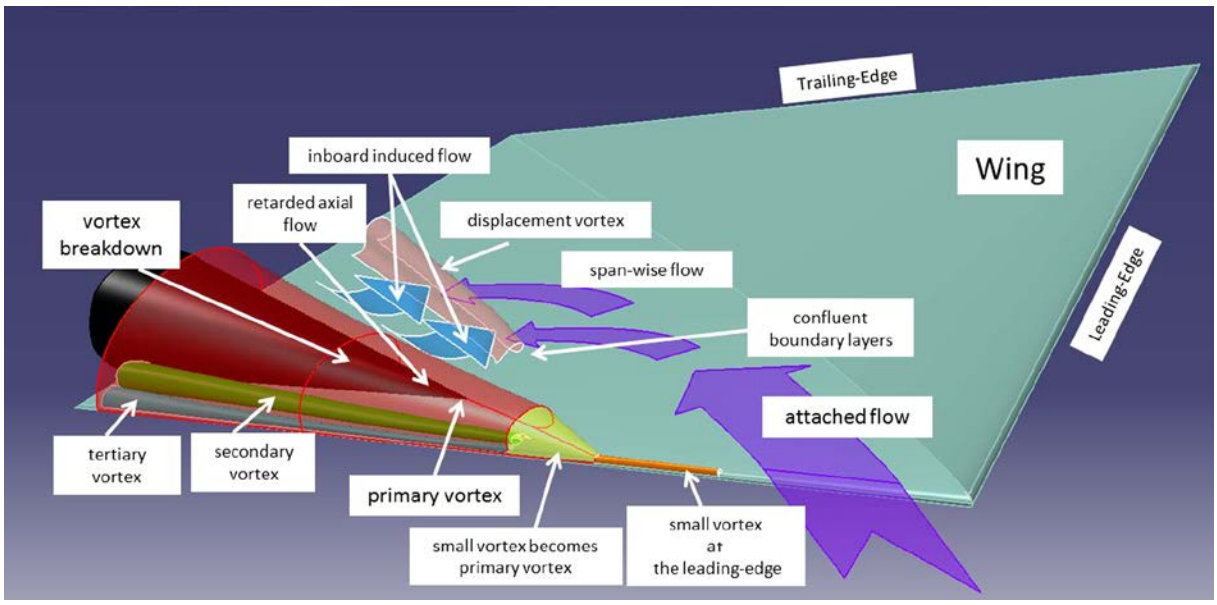

b) Sketch of flow separation characteristics at diamond wing blunt leading-edge [16]

Figure 16-9: Diamond wing near wall flow characteristics for blunt leading-edge incipient flow separation; φ_W = 53°, α = 12 deg, Re_{mac} = 2.7 x 10^6, Ma = 0.15.

3.3 Lambda Wing – Unsteady Aerodynamics

A diamond type or lambda type planform shape may be used for modern Unmanned Combat Aerial Vehicle (UCAV) designs. At higher angles of attack, medium to high sweep angles and combinations of round and sharp leading edges can lead to complex vortex systems. At higher free stream speeds, shocks may additionally occur. They have an impact on the development of the vortical flow and the resulting surface pressure distributions. For motions of the wing or dynamic deformations, strong variations of the pressure distributions arise. For subsonic speeds, the resulting unsteady pressure distributions related to the vortical flow exhibit strong time lags. The steady and unsteady surface pressure distributions at transonic flows are influenced by the motion of the shocks, the leading-edge vortices and the interaction between them and highly depending on the angle of attack. Therefore, experiments on unsteady aerodynamic effects associated with leading-edge vortex flow evolution are of particular interest.

In the Transonic Wind Tunnel (TWG) Göttingen, experiments have been carried out on a lambda wing type model undergoing pitch oscillations to study unsteady pressure distributions of vortex dominated flow including transonic effects [33]. The half wing model has a leading edge sweep angle of 53 deg and a half span of 0.51 m. The reference chord length is 0.3113 m. The IWEX (German acronym for: Unsteady Vortex Experiment) model consists of a lower and a slightly bigger upper shell manufactured from the aluminum zinc alloy 7075. The model has a round leading-edge with a constant nose radius to chord ratio of 0.5%.The free stream Mach number is varied between 0.3 and 0.7. Small pitching amplitudes of 0.08 to 0.4 deg at excitation frequencies up to 40 Hz are used. In particular, the data of unsteady Pressure Sensitive Paint (iPSP) and unsteady pressure sensor measurements are analyzed. Figure 16-10 depicts the real and imaginary part of the surface pressure fluctuations at a Mach number of 0.7 indicating the influence of shocks and induced flow separation and leading-edge vortex evolution around an angle of attack of 14 deg.

With increasing angle of attack, a suction peak and a shock occur near the leading edge. Then, a shock induced separation triggers the development of a vortex at the main wing. The unsteady pressures show that for lower angles of attack, the transonic influences are dominant. For higher angles of attack, the effect of the vortex becomes of similar magnitude and dominates the unsteady characteristics. The shock exhibits an inverse motion with increasing angle of attack. For angles of attack beyond the maximum lift, the unsteady pressure distributions and the lift show a significant phase lag already at very low oscillation frequencies. Compared to subsonic cases, the supersonic region shifts the vortex induced pressures downstream.

4. VORTICAL FLOW ANALYSIS – TRANSPORT AIRCRAFT WING

As a second vortex flow scenario regime, the evolution and development of the wake vortex system emanating from a transport aircraft wing is exemplarily discussed for the high-lift approach flight state.

The trailing vortex system of a transport aircraft at approach and landing is of particular interest with respect to flight safety. Consequently, the impact of this vortex system resulting in induced downwash or rolling moment on a follower aircraft has to be avoided. The knowledge on the evolution and interactions of the wake vortex system may be used to study means of wake vortex alleviation and decay [8]. Flow physics quantities from small–scale up to full–scale (free flight) experiments have been obtained during extensive measurement campaigns.

The wake near field of a transport aircraft in high lift configuration is characterized by a heterogeneous vortex system, Fig. 16-11. Here, a twin aisle aircraft half model (Λ = 9.30, λ = 0.29) in high lift approach configuration has been tested at an angle of attack of 7.0 deg. The configuration is equipped with inboard and outboard through-flow nacelles representing a four-engine airliner. Inboard, midboard and outboard slats are set at 19.6, 23.0, and 23.0 deg, respectively, inboard and outboard flaps are deployed at 26.0 deg and aileron setting is 5 deg. The horizontal tail plane is adjusted with –6.0 deg with respect to trimmed flight conditions for a lift coefficient of 1.44.

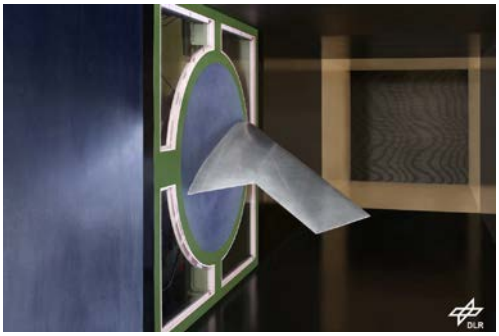

Lambda-type wing half model configuration installed in TWG wind tunnel test section side mounted on balance with turn table

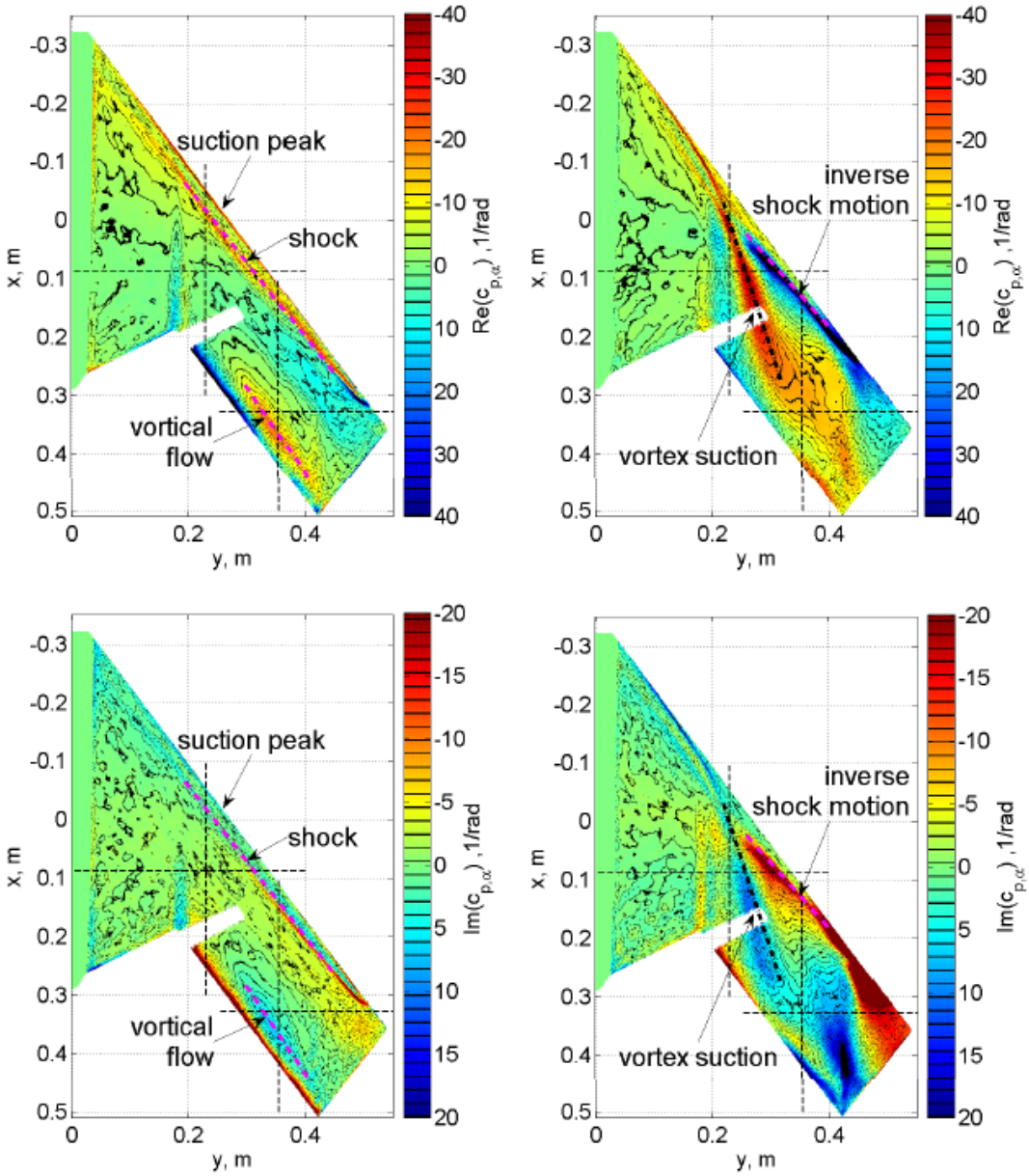

Figure 16-10: Lambda wing unsteady surface pressure distributions obtained with iPSP; Real and Imaginary part of fluctuations in surface pressure c_p at Ma = 0.7 and Re_{mac} = 1.8 x 10^6; left: α = 11 deg ± 0.2 deg, f = 36 Hz: dominated by transonic effects with incipient vortical flow; right: α = 14 deg ± 0.2 deg, f = 36 Hz; dominated by fully developed vortex; [33].

Figure 16-11 shows the transport aircraft wind tunnel half model and results for the measured non-dimensional axial vorticity distribution taken at several cross flow planes at stations x* = x/b = 0.02, 0.37, 1.0, 2.0, 3.0, 4.0, and 4.5. The wake vortex near field is characterized as follows (x/b = 0.02, 0.37): Besides the wing tip vortices, there are also vortices shed at the side edges of slats, flaps and ailerons. In addition, strong nacelle vortices develop due to the oblique flow on the nacelle caused by wing sweep and inclination. Further, nacelle strakes, slat horns, flap track fairings and other geometric discontinuities create a variety of concentrated vortices of smaller scale. Focusing on the dominant single vortices of the wing half span domain, the near field is typically characterized by six main vortices, namely the wing tip vortex (WTV), the outboard flap vortex (OTV), the outer and inner engine nacelle vortices (ONV and INV), the wing-fuselage vortex (WFV) and the horizontal tailplane vortex (HTV). The WTV, OFV, ONV, and INV have the same sense of rotation which is here of positive sign, i.e. positive vorticity or circulation, respectively, referring to the right wing of the lift producing configuration. The WFV and HTV are characterized by an opposite sense of rotation, or negative vorticity. For the WFV, this negative vorticity is caused by the change in the circulation gradient at the wing-fuselage junction, while for the HTV the tailplane produces negative lift with respect to a trimmed configuration. The dominant wing vortices are linked by the wing vortex sheet emanating from the trailing-edge due to the difference in the lateral velocities of wing upper and lower side. The evolution of the main near field vortices described above is also reflected by changes in the spanwise circulation gradient [8].

The near field wake vortex sheet is indicated in the cross flow plane by a lateral band of increased velocity fluctuations, Fig. 16-12. In addition to the turbulent wing boundary layer it results from the shear layer due to the difference in direction of the lateral velocities at the confluence of the wing flow from upper and lower side at the trailing edge. Further contributions to the turbulent wake are associated with local flow separation due to the wing geometric discontinuities (side edges, etc.) leading to the formation of large and small scale vortices. The lateral zone of increased turbulence intensity is clearly separated from the surrounding flow field. The latter show very low turbulence levels of about 0.5% according to free stream conditions while the turbulence levels of the wing vortex sheet are in the range of 5% - 7%. These levels characterize the intensities of the velocity fluctuations in axial, lateral and vertical direction. The overall spanwise patterns of the turbulence intensity fields in the three coordinate directions exhibit no significant differences but local variations can be detected at the areas of the embedded dominant near field vortices. At the plane of symmetry, the interfering turbulent boundary layers of wing and fuselage influence the wake vortex evolution creating a larger zone of increased turbulence intensity. Local turbulence maxima can be attributed to the dominant near field vortices where the turbulence peaks indicate the vortex cores. The turbulence intensities of the vertical velocity fluctuations reach levels of $Tu_z \approx 10\% - 13\%$ for the engine nacelle vortices (INV and ONV), $Tu_z \approx 7\% - 9\%$ for the flap vortex (OFV), and $Tu_z \approx 8\% - 9\%$ for the wing tip vortex (WTV). The gradients and curvatures in the mean axial and radial vortex velocity profiles contribute to the increase in turbulence, but also the phenomenon of “meandering” is of relevance representing random fluctuations of the vortex center around a mean position. While the velocity field distributions related to the results of Figures 16-11 and 16-12 are measured with multi-wire hot-wire probes to derive temporal cross correlations and to analyze turbulence spectra [8] the vorticity field distributions mapped in Figure 16-13 are taken from Stereo-PIV measurements.

Besides this large-scale vortex system vortices of smaller scales are associated with low-speed and high-speed stall. For high-speed stall, shock induced flow separation occurs at the rearward portion of the wing which may result in a severe dynamic impact on the wing structure, called transonic buffeting. Analyzing the latter, similarity in Reynolds number and Mach number is essential resulting in cryogenic wind tunnel testing. Consequently, PIV and iPSP techniques have to be adapted to cryogenic conditions leading to remotely controlled camera adjustments, parameter settings and conduction of measurements where a direct handling of the hardware involved is not possible. Further, relevant model paints for iPSP are needed. Only simultaneously running measurement procedures comprising time resolved forces and moments, surface pressure distributions, flow field quantities obtained by sophisticated optical techniques and model

deformations ensures a data base necessary for the relevant flow physics analysis and for cross comparison of results taken from scale resolving CFD methods.

Transport aircraft half model configuration mounted in closed wind tunnel test section

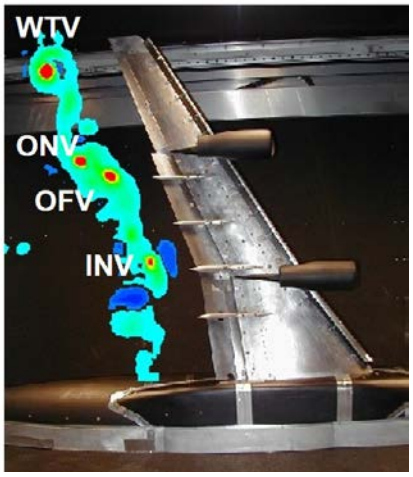

Indication of concentrated near field vortices in the wing wake vortex sheet emanating from wing tip, flap edge and through-flow nacelles (x* = x/b = 0.02)

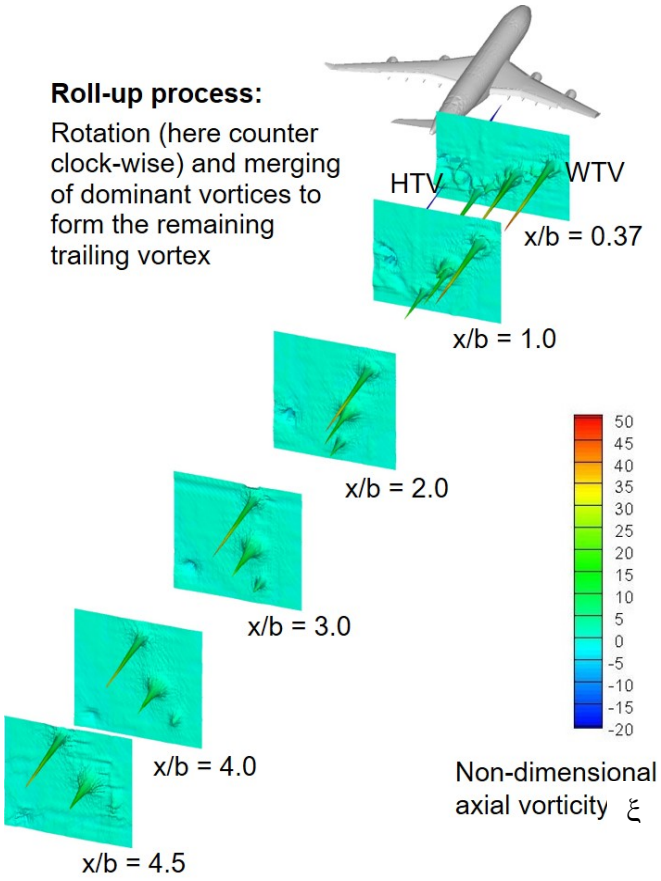

Figure 16-11: Wake vortex development in the extended near field for a transport aircraft model in high lift approach configuration indicated by non-dimensional axial vorticity patterns for several downstream cross flow planes; α = 7.0 deg, Re_{mac} = 0.525 x 10^6, Ma = 0.07; [8].

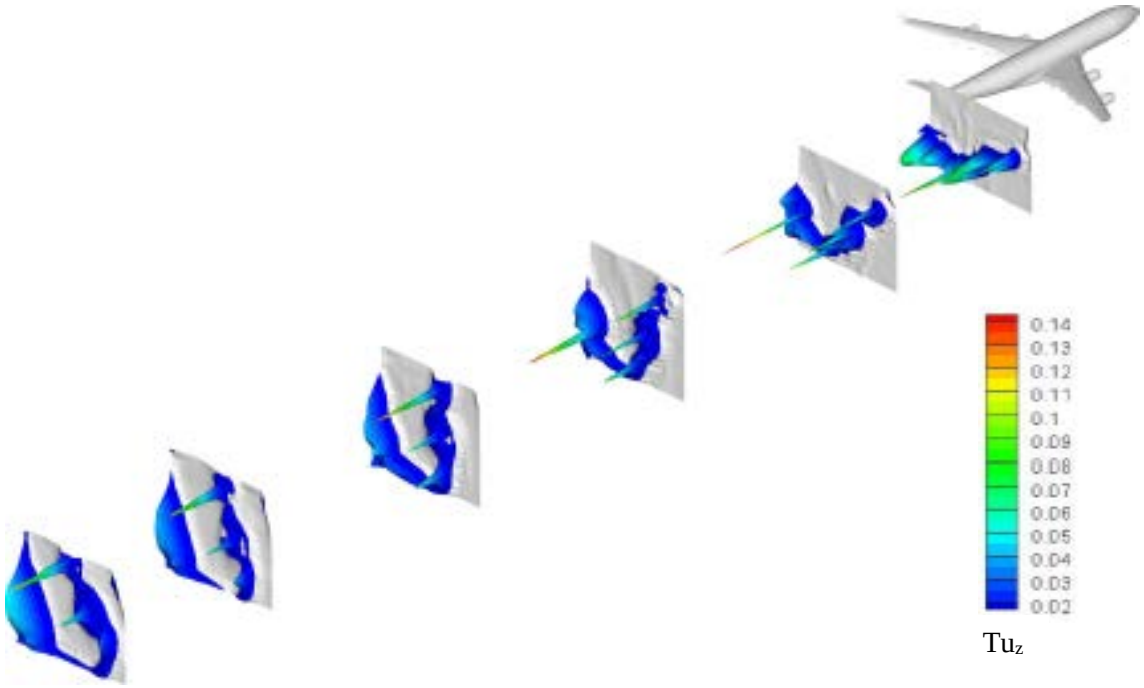

Figure 16-12: Wake vortex development in the extended near field for a transport aircraft model in high lift approach configuration indicated by turbulence intensity patterns related to vertical velocity fluctuations for several downstream cross flow planes; α = 7.0 deg, Re_{mac} = 0.525 x 10^6, Ma = 0.07; [8].

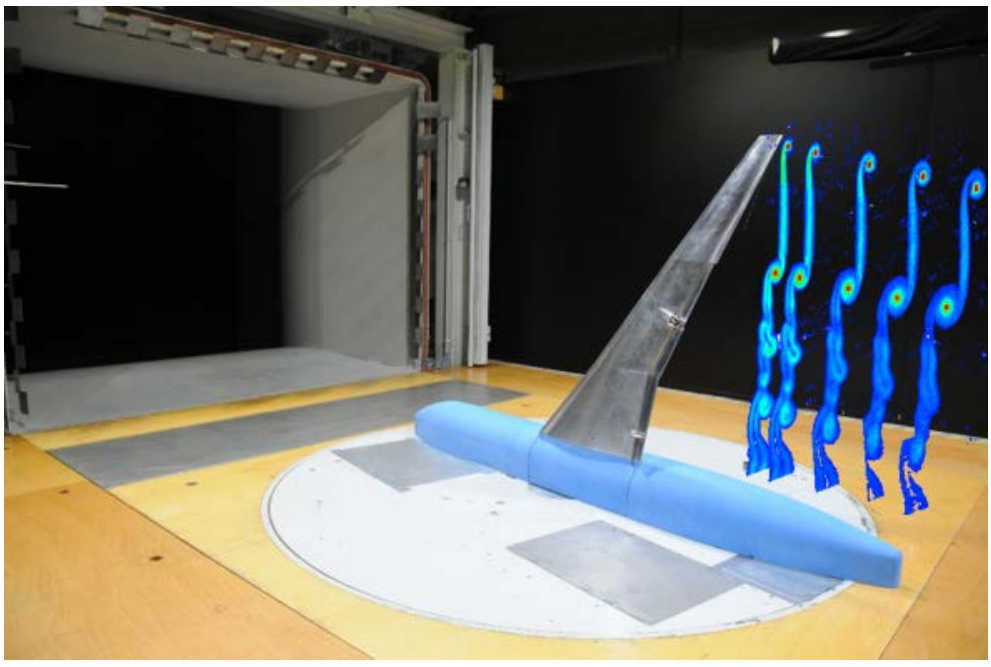

Figure 16-13: Wake vortex development in the near field for a single aisle transport aircraft model in high lift approach configuration indicated by patterns of vorticity magnitude obtained from Stereo-PIV measurements for several downstream cross flow planes; α = 7.0 deg, Re_{mac} = 0.5 x 10^6, Ma = 0.07.

5. CONCLUSION AND OUTLOOK

A brief survey has been given on wind tunnel testing and measurement techniques typically employed to capture aerodynamic forces and moments, surface pressure distributions, flow field velocities and pressures and near wall flow field quantities. Besides standard test techniques a focus is on non-intrusive optical measurements, such as Particle Image Velocimetry (PIV) and (unsteady) Pressure Sensitive Paint ((i)PSP) methods. A variety of application examples are discussed highlighting the potential of experimental aerodynamics in knowledge enhancement on complex flow physics. The use cases are dedicated to the flow separation development on swept leading edges with subsequent leading-edge vortex formation associated with low aspect ratio wings of delta, diamond and lambda planform type and the wake vortex flow field evolution of transport aircraft wings. Different separation scenarios are evaluated with special emphasis on unsteady characteristics which may cause dynamic loading on the aircraft structure.

The main interest of today's research in aerodynamics is directed to problems where unsteady and separated flows are predominant. For investigations of flow fields with pronounced spatial structures and/or rapid temporal or spatial changes, for example transition from laminar to turbulent flow, evolution of coherent vortical flow structures, shock induced flow separation, motion induced unsteady aerodynamics in subsonic and transonic flows, experimental techniques such as PIV and iPSP are required which allow to record velocity fields and surface pressure variations with sufficient spatial and temporal resolution. An important feature of such methods is that a reliable basis of experimental data is provided for direct comparison with high fidelity numerical calculations. The further development and application of PIV and iPSP for crogenic test conditions will significantly enhance the technical knowledge level for analyzing unsteady flow physics scenarios and mechanisms at flight Reynolds numbers.

Acknowledgements

The author highly appreciates the contributions of the former and present members of his research group to the scientific work documented herein as well as the fruitful cooperations within the NATO RTO/STO groups AVT-113, AVT-183 and others and all people involved.

BIBLIOGRAPHY

[1] AGARD (ed.), "Wind Tunnel Wall Corrections," AGARDograph AGARD-AG-109, NATO, 1966.

[2] AGARD (ed.), "Wind Tunnel Wall Corrections," AGARDograph AGARD-AG-336, RTO/NATO, 1998.

[3] AGARD (ed.), "Wall Interference, Support Interference and Flow Field Measurements," AGARD Conference Proceedings AGARD-CP-535, NATO, 1993.

[4] AGARD (ed.), "Assessment of Wind Tunnel Data Uncertainty," AGARD Advisory Report AGARD-AR-304, NATO, 1994.

[5] Beguin, B., Breitsamter, C., and Adams, N. A., "Aerodynamic Investigations of a Morphing Membrane Wing," AIAA Journal, Vol. 50, No. 11, 2012, pp. 2588-2599.

[6] Breitsamter, C., "Aerodynamic Active Control for Fin Buffet Load Alleviation," Journal of Aircraft, Vol. 42, No. 5, 2005, pp. 1252-1263.

[7] Breitsamter, C., "Unsteady flow phenomena associated with leading-edge vortices," Progress in Aerospace Sciences, Vol. 44, No. 1, 2008, pp. 48-65. doi: 10.1016/j.paerosci.2007.10.002.

[8] Breitsamter, C., "Wake vortex characteristics of transport aircraft," Progress in Aerospace Sciences, Vol. 47, No. 1, 2011, pp. 89-134.

[9] Breitsamter, C. and Laschka, B., "Velocity Measurements with Hot-Wires in a Vortex-Dominated Flowfield," Wall Interference, Support Interference and Flow Field Measurements, AGARD-CP-535, Brussels, Belgium, Oct. 4-7, 1993, pp. 11-1–11-13.

[10] Buzica, A., and Breitsamter, C., "Turbulent and transitional flow around the AVT-183 diamond wing," Aerospace Science and Technology, Vol. 92, No. 4, 2013, pp. 520-535. doi: 10.1016/j.ast.2019.06.025.

[11] Fonov, S., Jones, G., Crafton, J., Fonov, V., and Goss, L., "The development of optical techniques for the measurement of pressure and skin friction," Measurement Science and Technology, Vol. 16, 2005, pp. 1-8. doi: 10.1088/0957-0233/0/000.

[12] Furman, A., and Breitsamter, C., "Turbulent and unsteady flow characteristics of delta wing vortex systems," Aerospace Science and Technology, Vol. 24, No. 1, 2013, pp. 32-44. doi: 10.1016/j.ast.2012.08.007.

[13] Grawunder, M., Reß, R., and Breitsamter, C., "Thermographuc Transition Detection for Low-Speed Wind-Tunnel Experiments," AIAA Journal, Vol. 54, No. 6, 2016, pp. 2011-2015. doi: 10.2514/ 1.J054490.

[14] Haigermoser, C., Scarano, F., and Onorato, M., "Investigation of the flow in a circular cavity using stereo and tomographic particle image velocimetry," Experiments in Fluids, Vol. 46, 2009, pp. 517-526. doi. 10.1007/s00348-008-0577-2.

[15] Heckmeier, F. M., Iglesias, D., Kienitz, S., and Breitsamter, C., "An Innovative Development of a Five-Hole Pressure Probe for Highly Unsteady Flow Phenomena," Proceedings of ASME Turbo Expo 2019: Turbomachinery Technical Conference and Exposition, GT2019, Phoenix, Arizona, USA, June 17-21, 2019, pp. 1-12.

[16] Hitzel, S. M., Boelens, O. J., Rooij, M., and Hövelmann, A., "Vortex development on the AVT-183 diamond wing configuration – numerical and experimental findings," Aerospace Science and Technology, Vol. 57, No. 1, 2016, pp. 90-102. doi: 10.1016/j.ast.2015.12.007.

[17] Hövelmann, A., "Analysis and Control of Partly-Developed Leading-Edge Vortices," Dissertation, Technical University of Munich, Verlag Dr. Hut, ISBN 978-3-8439-2807-6, 2016.

[18] Hövelmann, A., Knoth, F., and Breitsamter, C., "AVT-183 diamond wing flow field characteristics Part 1: Varying leading-edge roughness and the effects on flow separation onset," Aerospace Science and Technology, Vol. 57, No. 1, 2016, pp. 18-30. doi: 10.1016/j.ast.2016.01.002.

[19] Hövelmann, A., Grawunder, M., Buzica, A., and Breitsamter, C., "AVT-183 diamond wing flow field characteristics Part 2: Experimental analysis of leading-edge vortex formation and progression," Aerospace Science and Technology, Vol. 57, No. 1, 2016, pp. 31-42. doi: 10.1016/j.ast.2015.12.023.

[20] Hummel., D., "The International Vortex Flow Experiment 2 (VFE-2): Background, objectives and organization," Aerospace Science and Technology, Vol. 24, No. 1, 2013, pp. 1-9. doi: 10.1016/j.ast.2012.08.008.

[21] Klar, J.-U., and Breitsamter, C., "Unsteady Aerodynamic Loads on a High-Agility Aircraft due to Wake Vortex Encounter," Journal of Aircraft, Vol. 51, No. 5, 2014, pp. 1511-1521. doi: 10.2514/1.C032388.

[22] Klar, J.-U., Breitsamter, C., Hickel, S., and Adams, N. A., "Integrated Experimental-Numerical Analysis of High Agility Aircraft Wake Vortex Evolution," Journal of Aircraft, Vol. 48, No. 6, 2011, pp. 2050-2058.

[23] Konrath, R., Klein, C., and Schröder, A., "PSP and PIV investigations on the VFE-2 configuration in sub- and transonic flow," Aerospace Science and Technology, Vol. 24, No. 1, 2013, pp. 22-31. doi: 10.1016/j.ast.2012.09.003.

[24] Laschka, B., Ranke, H., and Breitsamter, C., "Application of unsteady measurement techniques to vortical and separated flows," Zeitschrift für Flugwissenschaften und Weltraumforschung, Band 19, Heft 2, April 1995, pp. 90-108.

[25] Luckring, J. M., "Initial experiments and analysis of blunt-edge vortex flows for VFE-2 configurations at NASA Langley," Aerospace Science and Technology, Vol. 24, No. 1, 2013, pp. 10-21. doi: 10.1016/j.ast.2012.02.0005.

[26] Luckring, J. M., and Hummel, D., "What was learned from the new VFE-2 experiments," Aerospace Science and Technology, Vol. 24, No. 1, 2013, pp. 77-88. doi: 10.1016/j.ast.2011.07.012.

[27] Luckring, J. M., Boelens, O. J., Breitsamter, C., Hövelmann, A., Knoth, F., Malloy, D. J., and Deck, S., "Objectives, approach and scope for the AVT-183 diamond wing investigations," Aerospace Science and Technology, Vol. 57, No. 1, 2016, pp. 2-17. doi: 10.1016/j.ast.2015.12.023.

[28] Parsley, M.: The HALLCREST Handbook of Thermochromic Liquid Crystal Technology. Technical Report, HALLCRFST Products. Inc., 1820 Pickwick Lane, Glenview, Illinois 60025, U.S.A., Jan. 1991.

[29] Pope, A., and Goin, R. L., "High Speed Wind Tunnel Testing", John Wiley & Sons, ISBN 0-471-69402-9, 1966.

[30] Rae, Jr., W. H., and Pope, A., "Low Speed Wind Tunnel Testing", John Wiley & Sons, ISBN 0-471-87402-7, 1984.

[31] Smith, S. C., "Use of Shear-Sensitive Liquid Crystals for Surface FIow Visualization," Journal of Aircraft, Vol. 29, No. 2, 1992, pp. 289-293.

[32] Tropea, C., Yarin, A., and Foss, J. F., "Springer Handbook of Experimental Fluid Mechanics", Springer Verlag, ISBN 3-540-25141-3, 2007.

[33] Wiggen, S., Henne, U., Klein, C., Nuhn, J., and Sachs, W., " Unsteady surface pressures measured at a pitching Lambda wing with vortex dominated flow and transonic effects," CEAS Aeronautical Journal, Vol. 9, No. 3, pp. 417-427, 2018. doi. 10.1007/s13272-018-0239-4.